



Impact-induced convection as the main mechanism for formation of lunar mare basalts

Abdolreza Ghods¹ and Jafar Arkani-Hamed^{2,3}

Received 3 March 2006; revised 8 August 2006; accepted 8 September 2006; published 30 March 2007.

[1] Using a suite of numerical models, we show that impact-induced convection in the Moon can explain the formation of lunar mare basalts, the depth range of their source region, the observed delay between impact basin formation and starting time of mare flows, and the long duration of the basaltic flows. The effects of an impact on the thermal evolution of the Moon and melt production in the mantle are investigated using convection calculations in an axisymmetric cylindrical coordinate system. An ascending mantle plume is allowed to melt as it crosses the depth of the solidus temperature. We consider two different models: permeable and impermeable. Five different viscosity models and three different impact basin sizes are examined. The total amount of melt produced by the permeable model with 1000 times viscosity contrast across the computation domain is comparable to the observed mare flows in Imbrium and Orientale basins. Moreover, the starting time of major melting in the mantle and its duration are also compatible with the observations. The model also allows a rigid lithosphere to develop beneath the basins that is capable of supporting the mascons largely created during the peak mare flow period. The model for South Pole Aitken basin results in a substantial amount of melting in the mantle, which does not seem to be compatible with the observations. A potassium, rare earth elements, and phosphorus (KREEP) layer with high concentration of radioactive elements incorporated directly beneath the crust has minor effects on the melt production in the mantle.

Citation: Ghods, A., and J. Arkani-Hamed (2007), Impact-induced convection as the main mechanism for formation of lunar mare basalts, *J. Geophys. Res.*, 112, E03005, doi:10.1029/2006JE002709.

1. Introduction

[2] Lunar mare basalts cover most of the nearside impact basins, about 17% of the lunar surface. The basaltic flows occurred during 4–3.2 Gyr ago, within about 800 Myr after the formation of impact basins [e.g., Boyce, 1976; Geiss *et al.*, 1977], and major volcanic eruptions peaked in the Imbrian period (3.85–3.2 Gyr ago) [Nyquist and Shih, 1992; Head, 1976]. The volume of the volcanic flows in the basins ranges from 10^4 to 10^7 km³ [Solomon and Head, 1980]. The petrological evidence suggests source regions for mare basalts in the upper about 300 km of the lunar interior, on the basis of the assumption that mare basalts were saturated in pyroxene and olivine in the source regions [e.g., Heiken *et al.*, 1991; Longi, 1992]. A much deeper source region, about 500 km depth, is anticipated if the picritic glasses were genetically related to mare basalts [Delano and Livi, 1981]. Lunar mare basalts range in composition, space, and time with smaller and earlier

eruptions of high-Ti basalt, and larger and later eruptions of low-Ti basalt that were then followed by eruptions of high-Ti basalt [Cattermole, 1996].

[3] Two end-member mechanisms have been proposed for the formation of lunar basalts. One mechanism suggests that because of internal heating in the early history, deeper parts of the Moon partially melted, resulting in basaltic volcanism [e.g., Runcorn, 1974; Solomon, 1975]. The impact basins simply provided favorable depressions for basalt to pond. Because of no influence of the impacts on the formation of mare basalts, we call this mechanism passive. The absence of mare flows on the far side of the Moon, observed at the time, was related to a thick and low-density lunar crust [Solomon, 1975]. According to this hypothesis, basalt ascending from a deep-seated source ponded inside the thick crust of the far side when it reached the neutral buoyancy level. No association is expected between an intrusive and the surface morphology. However, such intrusive bodies would give rise to mascons when they are solidified, whereas all of the small mascons recently discovered in the far side of the Moon [Konopliv *et al.*, 1998] are associated with large craters. Moreover, the large crater Moscoviense in the far side is almost completely flooded and has an appreciable mascon. The passive mechanism also fails to explain the lack of substantial flooding in South Pole Aitken (SPA) basin, with a diameter of about 2500 km and a mean depth of about 8 km. The basin floor is

¹Institute for Advanced Studies in Basic Sciences, Zanjan, Iran.

²Department of Earth and Planetary Sciences, McGill University, Montreal, Quebec, Canada.

³Department of Physics, University of Toronto, Toronto, Ontario, Canada.

well below the equipotential surface that fits mare surfaces of the near side basins [Smith *et al.*, 1997; Arkani-Hamed *et al.*, 1999]. The basalt originated deep in the Moon is expected to fill the SPA basin before filling the nearside basins. The mechanism also cannot account for the longevity of the mare basalt volcanism, and the observed time lag of a few hundred million years between the formation of an impact basin and its flooding by mare basalts. In addition, the passive mechanism cannot explain the observed geochemical diversity of lunar basalts. In a partially molten zone deep in the mantle the melt accumulates at the top and creates chemically homogeneous basalt.

[4] The other mechanism, first proposed by Arkani-Hamed [1973, 1974] and further developed by Manga and Arkani-Hamed [1991], relates the basaltic volcanism to the effects of giant impacts on the thermal evolution of the Moon, hence the mechanism is called active. It is proposed that the impact related high-porosity ejecta blanket hampers heat loss from the upper mantle, and the intense heat generating a potassium, rare earth elements, and phosphorus (KREEP) layer directly beneath the crust causes partial melting in the upper about 200 km of the Moon beneath the low-conductivity ejecta blanket. The melt laterally migrates to the basin. The KREEP layer, rich in potassium, rare earth elements and phosphorus, is the product of the late-stage magma ocean solidification [e.g., Warren and Wasson, 1979]. The active mechanism successfully explains the observed amount of mare basalt and the time lag between the impact basin formation and the basaltic flow. The success of the mechanism relies on the assumption that heat transfer is by conduction alone, which allows the heat generated by the KREEP layer produce substantial melting. Despite its success the mechanism is not adequate, because at such a thermal state convection is not formidable in the lunar mantle. Any possible convection disperses heat from beneath the low-conductivity ejecta blanket and makes unlikely for the partial melting to occur. In addition, the mechanism does not explain the observation that some of the lunar basalts have come from much deeper interior. The mechanism also fails to explain the lack of significant mare flows in SPA basin.

[5] Wieczorek and Phillips [2000] argued that the KREEP layer was not global, but mostly limited within the so-called Procellarum KREEP Terrane. Using a pure conduction model generally similar to Manga and Arkani-Hamed's [1991] model, the authors showed that prolonged melting may occur in depths as great as 500 km. This is mostly because the authors used low thermal conductivity in their model, and assumed a high present bulk Uranium concentration of 24 ppb. However, the model suffers from serious internal inconsistencies, some of which has been pointed out by Elkins-Tanton *et al.* [2004]. For example, the model assumes a KREEP solidus temperature which allows total melting of the KREEP layer throughout the period of thermal evolution. However, because of static thermal conduction assumption, the model does not allow the molten KREEP layer to extrude as part of volcanism and thus eliminate the effects of the KREEP layer in heating the deep interior. In addition, the model does not consider impact effects, such as the removal of part of the KREEP layer, if not all, by excavation, and impact-induced thermal perturbations which create substantial lateral variations of

temperature in the upper parts of the mantle. Moreover, the model is not mechanically stable. Perturbations such as the impact shock wave and the lateral variations of temperature due to impact heating are sufficient to induce convection in the low-viscosity partially, or totally, molten mantle. We also note that it is highly unlikely that the relatively hot lithosphere and the partially to totally molten mantle beneath can support the mascon associated with Mare Imbrium for the last about 3 Gyr. Last but not least, although a thick KREEP layer can explain pervasive flooding in Imbrium basin and immediate surroundings, as demonstrated by Wieczorek and Phillips' [2000] model, there must be another mechanism independent of the KREEP layer to explain the mare flooding and appreciable mascons associated with other large impact basins, such as Crisium, Smytii, Nectaris, Orientale, and Moscoviense which are well outside the KREEP region. Mare Serenitatis, which is comparable in size to mare Imbrium, only partially overlies the KREEP region and yet it is totally flooded and has a mascon comparable to that of mare Imbrium.

[6] In support of the active mechanism and to explain the lack of mare flows in the SPA basin, Arkani-Hamed and Pentecost [2001] demonstrated that the convection introduced in the mantle by heating due to the giant impact was vigorous enough to strip away the KREEP layer from beneath the ejecta blanket and mix it with the entire interior of the Moon, thus preventing partial melting of the upper mantle beneath the blanket and formation of the mare basalt. The impact-induced mantle convection by smaller impacts that created Imbrium-size basins was weak and could not strip away the KREEP layer, rather it pushed the layer aside and created a thicker KREEP layer but farther than the ejecta blanket. The authors were concerned with the displacement of the KREEP layer by the mantle convection and did not investigate the effects of a thickened KREEP layer on the thermal state of the mantle. We show in this paper that impact-induced convection does not allow appreciable heating and partial melting beneath the ejecta blanket.

[7] A rather new version of the active mechanism is recently investigated by Elkins-Tanton *et al.* [2004], showing that an appreciable amount of basaltic melt is generated in the upper mantle by a large impact. The authors consider the in situ partial melting due to impact excavation which decreases the pressure in the mantle directly beneath the basin and thus suppresses the solidus temperature to deeper parts of the mantle causing partial melting in the uppermost mantle. Moreover, the subsequent isostatic uplift of the mantle creates localized convection and allows further partial melting. The impact heating in the upper mantle is not taken into consideration. About 98% of the total melt is produced by the in situ partial melting immediately after the impact, and only about 2% of the total melt is due to subsequent localized convection. This version of the active mechanism fails to explain the appreciable delay between the basin formation and the major basaltic volcanism [e.g., Boyce, 1976; Head, 1976; Geiss *et al.*, 1977], and also cannot explain the lack of volcanism for giant SPA impact basin.

[8] A successful mechanism for the formation of mare basalts should explain the observed volume of mare flows and the starting time and duration of the major volcanism.

Such a mechanism should also account for the effects of the impacts that created the large basins, namely excavation of large portion of the crust, subsequent isostatic uplift of the mantle, the low-thermal-conductivity ejecta blanket, impact-induced thermal perturbations, and possible whole mantle convection triggered by the impact-induced perturbations in the upper mantle.

[9] In this paper we examine the possibility that the whole mantle convection triggered by the impact perturbations [Ghods and Arkani-Hamed, 2004] is capable of producing large amounts of melt while explaining the time lag between the impact and the major basaltic flows as well as the long period of volcanism. The impact-induced convection in the mantle has also been proposed to explain the huge amount of volcanism required for the volcanic structure of Tharsis bulge of Mars [Reese *et al.*, 2002, 2004]. We determine the temperature in the lunar mantle at the impact time, assumed 4 Gyr ago, through the thermal evolution of the Moon starting at 4.6 Gyr ago, i.e., immediately after the accretion and crystallization of lunar magma ocean. The initial temperature at 4.6 Gyr ago is set at the solidus temperature of dry peridotite [McKenzie and Bickle, 1988]. We take into account the increase in the solidus temperature of the solid residue depending on the amount of partial melting. We then add the impact-induced temperature perturbations to the laterally averaged temperature immediately before the impact to obtain the initial temperature for the postimpact thermal evolution calculations. We also set the mantle velocity to zero at this time. This allows us to investigate the effects of an impact on the subsequent mantle convection. Different sets of models are considered in order to explore the effects of different physical parameters on the volume and time evolution of melt production, such as temperature-dependent thermal conductivity and viscosity, increase of the viscosity of the solid residue, distribution of radioactive heat generating elements, melt migration inside partially molten zones in the mantle, and the impact size.

2. Impact-Induced Thermal Convection

[10] The impact of a large projectile causes thinning of the crust, immense ejecta production, heating of the crust and upper mantle, in situ melting in the mantle, and formation of an impact basin. Such an impact may induce four stages of melting at different depths and times. The first occurs near the surface, by strong heating of the projectile and target that results in melting and vaporization of a major part of the projectile and the near-surface part of the target. This rapid melting does not create mare basalt. The second is the almost immediate in situ melting that occurs because of (1) the depressurization of the upper mantle by impact excavation of the crust which displaces the solidus to deeper parts of the mantle and (2) the impact heating. The third melting may occur by localized convection initiated by the subsequent isostatic uplift of the mantle directly beneath the basin. The materials from deeper parts of the upper mantle move upward and melt as they cross the depth of mantle solidus. The melting may occur in rather shallow depths. This localized convection together with the impact-induced thermal perturbations in the upper mantle beneath the basin may develop whole mantle convection, resulting in the

fourth stage of melting. The development of the whole convection and its associated partial melting may take a considerable amount of time, resulting in the observed delay of 100–800 Myr of mare flows relative to the time of the basin formation [e.g., Boyce, 1976; Geiss *et al.*, 1977]. The volume of the melt produced by the partial melting of the lunar mantle depends on many physical parameters such as the impact size and the initial temperature and composition of the mantle.

[11] We calculate several thermal evolution models of the Moon with different values of the physical parameters to investigate the timing and melt volume of the delayed fourth stage of melting of the mantle. Each model has a preimpact and a postimpact history. A preimpact model starts at 4.6 Gyr ago, immediately after the Moon chemically differentiated and the magma ocean solidified, and ends at 4 Gyr ago. It provides a reasonable starting temperature, composition, and melt depletion region (the region that has previously been partially melted and basaltic melt has been extracted) in the mantle prior to the climax time of impact event at 4 Gyr ago [e.g., Boyce, 1976; Geiss *et al.*, 1977]. The dry peridotite solidus [McKenzie and Bickle, 1988] is adopted as the initial temperature of the preimpact models. The initial temperature of a postimpact model consists of the laterally averaged (analogous to spherically symmetric in the spherical coordinate) part of the temperature distribution of the corresponding preimpact model immediately before the impact, and the impact-induced thermal perturbations plus the thermal perturbations due to the subsequent isostatic rebound of the mantle. Similarly, the initial depletion field of the postimpact model is the laterally averaged part of the depletion field of the corresponding preimpact model immediately before the impact, plus the depletion fields produced by the second and the third stages of melting mentioned above. Also, a postimpact model inherits all of the physical parameter values and boundary conditions from the corresponding preimpact model. The initial velocity field of the postimpact model is set to zero in order to investigate the mantle convection that is solely induced by the impact.

[12] The thermal evolution and melt production of the preimpact and postimpact models are calculated in an axisymmetric cylindrical coordinate system with a height of 1288 km and an aspect ratio (diameter/height) of 4. An aspect ratio of 8 is used for modeling the effects of a SPA-size impact. The equations of conservation of mass, momentum and energy are solved for a two-phase flow model with internal heating by radioactive elements, while allowing partial melting of the mantle in both preimpact and postimpact models. The equations are based on McKenzie's [1984] and Bercovici *et al.*'s [2001] derivations, but are modified to take into account the effect of melt extraction. The nondimensionalized governing equations are [Ghods and Arkani-Hamed, 2000],

$$-\frac{\partial \phi}{\partial t} + \nabla \cdot ((1 - \phi) \vec{V}^s) = 0, \quad (1)$$

$$\frac{\partial \phi}{\partial t} + \nabla \cdot (\phi \vec{V}^l) = \Gamma_e, \quad (2)$$

$$\nabla\Pi = \nabla((1 - \phi)\sigma) + Ra((\rho_s - \rho_s^o) + \phi(\rho_s - \rho_l))\delta_{i3} \quad (3)$$

$$\vec{V}^l - \vec{V}^s = -A\frac{K_\phi}{\phi}(\nabla\Pi + Ra(1 - \rho_l)\delta_{i3}) \quad (4)$$

$$\begin{aligned} \rho_s C_P^s \frac{\partial T}{\partial t} + \rho_s C_P^s ((1 - \phi)\vec{V}^s + \phi\vec{V}^l) \cdot \nabla T \\ = \frac{1}{Pe} \nabla \cdot (K\nabla T) + Di T((1 - \phi)V_z^s + \phi V_z^l) \end{aligned} \quad (5)$$

where t is time, \vec{V}^s is solid matrix velocity, \vec{V}^l is melt velocity, Π is perturbations to the hydrostatic pressure, ρ_s is density of the solid matrix, ρ_l is density of the melt, and K is thermal conductivity of solid matrix and melt. The hydrodynamic pressure is defined as $P = \Pi + \rho_s^o g \delta_c \delta_{i3}$ where g is the gravitational acceleration at the surface of the Moon, ρ_s^o is reference density of the solid matrix, δ_c is the characteristic length over which compaction occurs, and δ_{i3} is Kronecker delta function. In the momentum equation for the solid matrix, equation (3), it is assumed that pressure difference between the solid residue matrix and melt leads to an instantaneous volumetric deformation. For example, compaction occurs if the solid matrix pressure is larger than the melt pressure. The difference between the solid matrix and melt pressures, ΔP , is approximated by a linear volumetric deformation of the solid matrix as $\Delta P = \zeta \nabla \cdot \vec{V}^s$. The bulk viscosity of the two-phase flow media, ζ , is assumed to be equal to the viscosity of the solid matrix, η_s . The stress tensor for the solid matrix σ is defined as

$$\sigma = \eta_s \left[\nabla \vec{V}^s + (\nabla \vec{V}^s)^T \right] + (\zeta - 2/3\eta_s)(\nabla \cdot \vec{V}^s)\mathbf{I} \quad (6)$$

where \mathbf{I} is the unit matrix. Equations (1) and (2) express the conservation of mass of the solid matrix and melt, their densities are assumed to be constant. The density of the solid matrix (ρ_s) is not, however, constant in the momentum equation for the solid matrix, equation (3). Permeability, K_ϕ , is assumed to be a function of melt fraction, ϕ ,

$$K_\phi = 10^{-3} a^2 \phi^3 \quad (7)$$

where a is the grain size [Von Barga and Waff, 1986; Cheadle, 1993]. Equation (7) implicitly assumes that porosity network is interconnected at all melt fractions which is in good agreement with experimental results [Kohlstedt, 1992].

[13] Melting is a chemical reaction which depletes iron content and reduces the density of the solid residue. Therefore the density of the solid matrix, ρ_s , is a function of temperature, T , and volumetric fractional depletion induced by melting, \mathcal{M} ,

$$\rho_s = \rho_s^o (1 - \alpha(T - T_o) - \beta\mathcal{M}) \quad (8)$$

where α and β are the coefficients of thermal expansion and melt depletion, respectively. T_o is the reference temperature, assumed to be the average of the temperatures at the top and bottom of the computational domain. Equation (6) is stress-

strain constitutive law for compressible media where η_s is shear viscosity of solid matrix. Equation (4) is the momentum equation for the melt which is equivalent to Darcy's law. In the momentum equations the nondimensional number $Ra = (\rho_s^o g \delta_c^2) / (\eta_s^o W_o)$ corresponds to the conventional Rayleigh number in that it describes the strength of the thermal buoyancy force, $\rho_s^o g \delta_c^2$ versus the viscous force $\eta_s^o W_o$, where ρ_s^o , η_s^o and W_o are the reference density of the solid matrix, the reference viscosity of the solid residue and the characteristic velocity of the melt, respectively. Equation (3) is the momentum equation for the solid matrix. The first term on the right-hand side is the resistive force due to a compressible two-phase flow media and the second term is related to the thermal, chemical and melt retention buoyancy forces. The nondimensional number $D = (\eta_s^o K_\phi^o) / (\eta_l \delta_c^2)$ in equation (4) denotes efficiency of melt migration where K_ϕ^o and η_l are the reference permeability of the solid matrix and the viscosity of the melt (assumed 1 Pa s), respectively. Equation (5) is the conservation of energy where T represents temperature. In writing the energy equation, it is implicitly assumed that thermal equilibrium exists between the melt and solid matrix that are in immediate contact. We also assume that $\rho_l C_P^l = \rho_s C_P^s$ where C_P^s and C_P^l are the specific heat of the solid matrix and the melt. The nondimensional Peclet number $Pe = (W_o \delta_c) / (\kappa_s^o)$ describes the ratio of the rate of thermal advection to the rate of thermal diffusion, where κ_s^o is the thermal diffusivity of the melt and solid matrix. The nondimensional number $Di = (g \alpha \delta_c) / (C_P^s)$ is the dissipation number, quantifying importance of the adiabatic cooling/heating due to vertical velocity of the solid matrix, V_z^s , and melt, V_z^l .

[14] In the above formulation, a lunar mantle model consists of two incompressible continuous media, a solid residue matrix and melt contained in the matrix. However, the entire mantle is compressible because a given partially molten region compacts if melt migrates out and expands if melt migrates in from elsewhere. We consider adiabatic cooling/heating in our energy equation. At the end of each time step the temperature field is corrected to take into account the latent heat of melting. The thermal expansion, melt depletion (equation (8)) and melt retention (equation (3)) buoyancies are the three sources of buoyancy considered in our momentum equation.

[15] An iterative control volume method [Patankar, 1980] is adopted to solve the equations of mass, momentum and energy conservation for a two phase flow media, namely solid residue matrix and melt. The equations are solved over a grid of 441 and 241 in radial and vertical directions, respectively. Grid spacing in the vertical direction is fine and variable, varies between 1 and 5 km in the top 300 km of the model, but it is constant (i.e., about 7.7 km) in the lower part. A constant grid spacing of about 5.8 km is used along the radial direction. Details of numerical and mathematical formulations are given by Ghods and Arkani-Hamed [2000, 2002].

[16] Figure 1 shows the dimensions of the computational domain, and the boundary conditions used in the models. An initial crustal thickness of 30 km, and a temperature-dependent viscosity model are adopted. The adopted rheology allows for the growth of a cold stagnant layer at the top of the domain, more than 60 km at 4 Gyr ago. Accordingly,

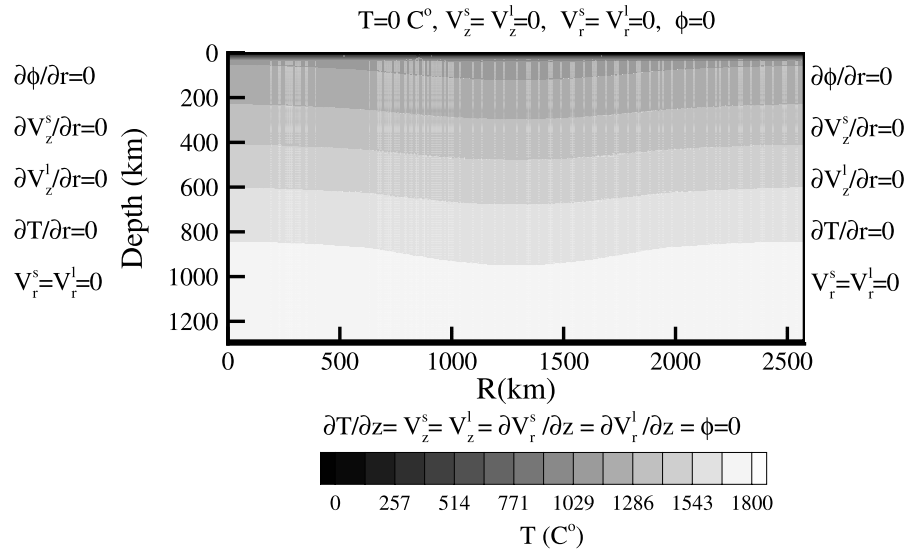


Figure 1. Initial temperature of the preimpact models and boundary conditions used in this paper. V_r^s , V_z^s , V_r^l , V_z^l , ϕ , and T are the horizontal and vertical components of the solid matrix velocity, the horizontal and vertical components of the melt velocity, melt fraction, and temperature, respectively; r and z are the cylindrical coordinates.

a stagnant rigid top boundary and a free slip bottom boundary are considered. The axis of symmetry (the right boundary) and the vertical wall of the cylindrical domain (the left boundary) are reflecting for both temperature and vertical component of velocity. The radial component of velocity is set to zero at these boundaries. Surface temperature is considered to be 0°C and a zero heat flux is assumed at the bottom boundary, because of a very small lunar core (about 300 km radius) and negligible heat flux to the mantle. The initial temperature distribution for preimpact models is also shown in Figure 1, which follows the solidus of dry peridotite of *McKenzie and Bickle* [1988] (Figure 2). It is slightly hotter in the lower mantle than that of the hot model of *Spohn et al.* [2001]. The initial temperature in the crust linearly decreases to zero at the surface. The initial temperature is slightly (a maximum of 30°C) perturbed by a cosine function to initiate convection. The results of the postimpact models, the main concern of our study, are not sensitive to the initial temperature perturbations of the preimpact models. Both cosine and white noise perturbations of the same maximum amplitude result in very similar postimpact thermal evolution for the preferred models. This is largely because we use the laterally averaged temperature and melt depletion fields of the preimpact models immediately before the impact together with the impact-related perturbations as the initial conditions for the postimpact models.

[17] Table 1 lists the values of the physical parameters used in our models. We assume a constant thermal expansion coefficient, and adopt the experimental temperature-dependent thermal conductivity of dry olivine by *Schatz and Simmons* [1972]. Current models of the distribution of heat-generating radioactive elements in the lunar crust and mantle vary significantly. In one extreme, some models allocate a value of 43% of the Moon's bulk radiogenic elements to the mantle [*Schubert et al.*, 1980] and on the other end it is suggested that 85% of the radiogenic

elements have been differentiated upwardly [e.g., *Binder and Lange*, 1980]. In our models, unless stated otherwise, the radioactive content of the crust is set to 25% of the total radioactive content of the Moon. We also consider a KREEP layer of 20 km thickness directly beneath the crust which contains 65% of the total radioactive content of the Moon. The grid spacing used in our models requires such a thick layer to accurately resolve the KREEP layer. The remaining radioactive elements are uniformly distributed in the mantle. A present bulk Uranium concentration of 17 ppb is considered [*Warren and Rasmussen*, 1987]. The present potassium to uranium and thorium to uranium ratios are set to 2000 and 4, respectively.

[18] We modified *McKenzie and Bickle's* [1988] batch melting model for fertile dry peridotite, by replacing the batch melting liquidus by the liquidus of pure forsterite (T_l^o). The modified melting model is used in the fractional melting of the lunar mantle in our preimpact and postimpact models. With melting temperature considerably higher than that of batch melting liquidus [*Presnall and Walter*, 1993], forsterite is the last refractory mineral of upper mantle rocks to melt. Our modification results in a lower rate of fractional melting of the upper mantle rocks. The relationship between the liquidus, T_l^o , and pressure is expressed as

$$T_l^o = 2164 + 4.77P_H \quad (9)$$

where P_H is the hydrostatic pressure in GPa. Changes in P_H due to melting are minute and are neglected in our calculations. The solidus of the fertile peridotite, T_s^o , is obtained by fitting a third-order polynomial to *McKenzie and Bickle's* [1988] solidus,

$$T_s^o = 1374.33 + 129.46P_H + 5.89P_H^2 - 1.59P_H^3, \quad (10)$$

The solidus and liquidus in equations (9) and (10) are in K. Our fractional melting assumes a linear relationship

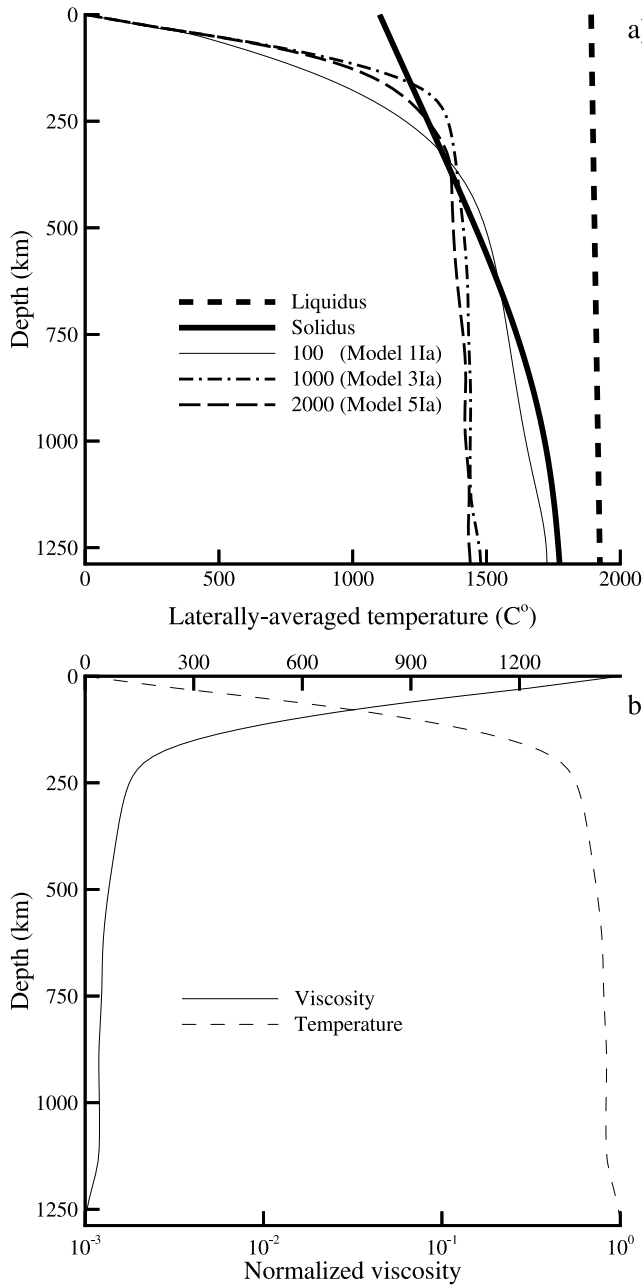


Figure 2. (a) Laterally averaged temperature profiles at 4 Gyr ago, immediately before an impact, for impermeable models with viscosity contrast of 100 (model 1Ia), 1000 (model 3Ia), and 2000 (model 5Ia). Solidus (bold curve) and liquidus (dashed bold curve) of dry peridotite are also shown. (b) Laterally averaged temperature and viscosity profiles for model 3Ia. The top and bottom horizontal axes show the laterally averaged temperature and normalized viscosity, respectively.

between the temperature and the fraction of melt depletion (\mathcal{M}),

$$\mathcal{M} = \frac{T - T_s^o}{T_l^o - T_s^o}. \quad (11)$$

a) [19] To account for the dynamic nature of the models, the \mathcal{M} field is advected in each time step using the following pure advection equation,

$$\frac{\partial \mathcal{M}}{\partial t} + ((1 - \phi)\vec{v}^s + \phi\vec{v}^l) \cdot \nabla \mathcal{M} = 0 \quad (12)$$

[20] For permeable models, where melt can migrate, ϕ is very different from \mathcal{M} . The fraction of melt produced in a given time step, $\Delta \mathcal{M}$, is computed by the following coupled equations,

$$\begin{aligned} \rho_s C_P T_1 &= \rho_s C_P T_2 + \Delta \mathcal{M} H, \\ \Delta \mathcal{M} &= \frac{T_2 - T_s}{T_l^o - T_s} (1 - \mathcal{M}), \end{aligned} \quad (13)$$

where T_1 and T_2 are temperatures before and after correcting for the melting effect, respectively. The latent heat of fusion H and the specific heat at constant pressure C_P are constant. T_s is the instantaneous solidus of the solid residue at the previous time step which is calculated using Equation (11) and setting $T_s = T$ to account for the increase of T_s through melting. The removal of melt in the fractional melting models increases T_s because the solid residue becomes more refractory. The temperature field is corrected for the absorption of the latent heat of fusion and $\Delta \mathcal{M}$ is added to the ϕ and \mathcal{M} fields. We use the monotonic second order upwind (MSOU) method [Sweby, 1984] to advect the melt depletion and the melt fraction fields.

[21] In the impermeable models, the portion of melt exceeding the 3% by volume threshold is extracted, assuming that at percentages above this threshold the melt can easily migrate within a partially molten zone. In permeable models, the melt moves slowly inside the partially molten porous solid residue matrix regardless of its percentage volume, but cannot penetrate in to the surrounding completely solid regions of the convecting mantle. However, when the melt enters the brittle part of the lithosphere it moves much faster through the lithosphere via fractures and veins [e.g. Nicolas, 1990; Ceuleneer and Rabinowicz, 1992]. We simulate the fast melt migration in the lithosphere by considering a melt extraction region of 90 km thick beneath an impact basin. It is thicker than the rigid outer parts of our models in order to have access to the partially molten zone in the upper mantle for melt extraction purposes. The permeable models are more realistic compared to the impermeable ones. Allowing differential motion of the melt relative to the solid residue matrix in the permeable models provides estimates of the effects of high-melt-fraction zone at the top of a mantle plume on the dynamics and partial melting of the plume. The melt in the extraction region that is in excess of 5% by volume is instantaneously extracted. It is assumed that at 5% melt percentage threshold, magma-induced fracturing and fast melt migration occur within the brittle part of the lithosphere. Melt extraction compacts the partially molten regions, and enhances mantle upwelling and the rate of melting. The dynamical effects associated with the melt extraction are included in the models by adding melt extraction rate Γ_e to the equation of conservation of melt, equation (2). In order to conserve mass in the computational domain, the bottom boundary is allowed to be partially open to balance the mass reduction due to the melt extraction. A constant inflow velocity is set at the bottom boundary so

Table 1. Physical Parameters Used in This Paper

Parameter	Value
Model height	1288 km
Model aspect ratio	4, 8
Initial thickness of crust	30 km
Reference solid density ρ_s	3300 kg m ⁻³
Melt density	2700 kg m ⁻³
Moon gravity	1.62 m s ⁻²
Reference viscosity of solid matrix η_o	10 ²² , 10 ²³ , 10 ²⁴ Pa s
Viscosity of melt	1 Pa s
Reference thermal conductivity	4.0 W m K ⁻¹
Specific heat C_p	1200 J kg ⁻¹ K ⁻¹
Grain size a	1 mm
Latent heat of melting H	1.2 × 10 ⁹ J m ⁻³
Thermal expansion coefficient α	3 × 10 ⁻⁵ K ⁻¹
Melting expansion coefficient β	0.024 ^a
Surface temperature	273 K
Present average uranium content	17 ppb
Present potassium to uranium ratio	2000
Present thorium to uranium ratio	4
KREEP layer thickness	20 km
Percentage of radioactive elements in the crust and KREEP layers	90%, 65%
Impact basin diameter D_o	200, 300, 600, 1200, 2400 km
Impact velocity	18 km/s
Percentage of partitioning of impact energy to heat energy	40%, 20%
Transition diameter from simple to complex crater D_*	15 km
Maximum impact basin excavation depth = 0.05 D_o	km
Distance of heat distribution normalized to crater radius	1.5
Ejecta/excavated volume ratio	0.8
Width of ejecta blanket = D_o	km
Thermal conductivity of ejecta	0.5 W/m/K

^aSparks and Parmentier [1994].

that the total mass entered into the computational domain within a given time step equals to the mass of the extracted melt. Opening of the bottom boundary does not introduce significant effects on the general pattern of mantle convection, because the ratio of the melt extracted within a time step to the entire volume of the domain is very small. Even for the extreme case of volcanism, the total extracted melt is less than 1% of the entire volume of the domain.

[22] At the end of each time step, the temperature field is checked for new melting, and the corresponding instantaneous solidus is determined. The melt depletion field and the KREEP layer are traced by solving the respective advection equations using the MSOU method, and the heat generation rate is updated on the basis of the characteristic decay constants of different radioactive elements.

3. Impact Effects

[23] The initial temperature distribution for a postimpact model consists of the laterally averaged temperature distribution of the corresponding preimpact model and the impact-induced temperature perturbations, calculated following the technique used by Mohit and Arkani-Hamed [2004]. We first determine the impact-induced shock pressure inside the crust and mantle, and then use the pressure field to determine the thermal energy deposited by the shock pressure. Briefly, the observed basin diameter, D_o , is related to the transient diameter of the basin, D_{tr} , using Holsapple's [1993] scaling relationship,

$$D_{tr} = 0.7576 D_o^{0.921} D_*^{0.072} \quad (14)$$

where D_* is the transition diameter from simple to complex crater, assumed 15 km for the Moon [Melosh and Ivanov,

1999]. The transient diameter is then related to the kinetic energy of the projectile, E , through Schmidt and Housen [1987] relationship,

$$E = \left(\frac{D_{tr} U^{0.09} g^{0.22}}{0.2212} \right)^{\frac{1}{0.26}} \quad (15)$$

where g is the gravitational acceleration at the surface of the Moon and U is the projectile velocity, set to 18 km/s [Ivanov, 2001]. Assuming a spherical projectile of basaltic composition, with density 3000 kg/m³, the projectile kinetic energy is related to its radius, R_{pr} , which in turn is related to the radius of the isobaric core, $R_o = 0.75 R_{pr}$, and the penetration depth of the projectile, assumed equal to R_{pr} [e.g., Pierazzo et al., 1997]. The Hugoniot equation [Melosh, 1989]

$$P_o - P'_o = \rho u_s u_p \quad (16)$$

together with a power law distribution of shock pressure outside the isobaric core

$$P(r) = P_o \left(\frac{r}{R_o} \right)^{-n}, \quad r > R_o, \quad (17)$$

and the empirical relationship between the particle velocity, u_p , and shock wave velocity, u_s ,

$$u_s = C + s u_p \quad (18)$$

yield the shock pressure, $P(r)$, as a function of distance r from the center of the impact crater (the impact site) and the

pressure in the isobaric core, P_o . The unshocked pressure P'_o is assumed to be negligible compared to the isobaric core pressure. C is the bulk sound speed ($= 3$ km/s) and s ($= 1.5$) is the shock parameter of the material [Melosh, 1989]. A constant n value of 1.87 [Melosh, 1989] is adopted. Also the pressure reduction near the surface due to interference of the direct and reflected waves [Melosh, 1989] is taken into consideration.

[24] As shock wave passes, the target decompresses adiabatically and a large percentage of the deposited energy is released as kinetic energy (i.e., excavation of the crater). The remaining energy goes mostly into “waste heat” [Bjorkman and Holsapple, 1987], which can be estimated for the regions with low shock pressure [Melosh, 1989, pp. 43–44]. At the projectile velocity adopted in this study about 35–55% of the impact energy can be partitioned into heat [O’Keefe and Ahrens, 1977]. We partition 40% of the impact energy to heat energy. Following Melosh [1989], we determine the temperature increase due to impact heating in the region with shock pressures lower than 10 GPa. An exponential function is then employed to extrapolate temperature values between this region and the isobaric core at the impact site, where the temperature is assumed to be constant.

[25] The vast cavity created by a large projectile is subsequently filled, partly by the fall backs of the excavated material and slumping of the walls almost immediately, but largely by the isostatic upwelling of the mantle directly beneath the excavated region within a geologically short time period. To take into account the thermal effects of the isostatic uplift of the mantle, we first calculate the temperature distribution immediately after the impact and prior to mantle uplift, by adding the preimpact laterally averaged temperature and the temperature increase by the impact heating described above, and then vertically displace the temperature distribution as required by the uplift. The uplift is simulated by shifting up the upper mantle beneath the impact-induced cavity to retain Airy isostatic equilibrium. The preuplift cavity volume is assumed parabolic with the maximum depth equals to 0.1 of the cavity diameter. A crustal density of 2800 kg/m³ and mantle density of 3400 kg/m³ are used to determine the isostatic uplift. The upward shifting is performed only in the upper 300 km of the mantle and on a grid interval of 1 km. The resulting modified temperature field is then interpolated to the mesh used in our thermal evolution calculations.

[26] A large Imbrium-size impact results in a basin of a few kilometers depth after the isostatic adjustment, because of denser mantle compared to surrounding crust. Also a continuous ejecta blanket of a few hundred meters thickness covers the immediate surrounding area to some distance. The geometry of the computational domain of the thermal evolution models does not allow for explicit inclusion of the basin depth and the ejecta blanket height. Although the crust may not partake in mantle convection because of very high viscosity, the resulting surface topography does affect the temperature in the crust and to some extent in the uppermost mantle. We ignore the geometry of the surface topography produced by the impact by keeping the surface flat, but incorporate the topographic effects on the thermal evolution models by modifying the thermal conductivity and heat generation in the crust. An infinite thermal conductivity and

zero heat generation are assumed for the empty space of the basin to assure that the temperature at the basin floor is actually the surface temperature, and no radioactive heating exists in the empty space. The modified thermal conductivity K'_c of the crust beneath the basin is determined by

$$K'_c = \frac{K_c h_c}{h_c - h_b} \quad (19)$$

and the modified rate of heat generation H'_c is obtained from

$$H'_c = \frac{H_c(h_c - h_b) + H_m h_m}{h_c} \quad (20)$$

where h_c , K_c , and H_c are the thickness, the mean thermal conductivity, and the rate of heat generation of the surrounding crust. h_b , and h_m are the basin depth and the thickness of the mantle uplift, and H_m is the rate of heat generation in the mantle.

[27] For the effects of the ejecta blanket, we approximate the blanket by a continuous annulus with a width equal to the radius of the basin and a triangular height decreasing from the basin rim outward. The blanket contains 80% of the excavated rocks. The rest of the excavated rocks are distributed discontinuously, producing rays of ejecta that have little effects on the thermal state of the Moon. The modified thermal conductivity K'_c of the crust beneath the ejecta blanket is calculated from

$$K'_c = \frac{h_c}{(h_j/K_j + h_c/K_c)} \quad (21)$$

and the modified rate of heat generation H'_c in the crust is determined by

$$H'_c = \frac{H_c h_c + H_j h_j}{h_c} \quad (22)$$

where the index j stands for the ejecta. We use 0.5 W/m/K for the thermal conductivity of the porous ejecta blanket, which is a factor of 8 smaller than the thermal conductivity of the crust. Heat generation in the ejecta layer, H_j , is assumed to be equal to H_c . Also, no KREEP layer is considered directly beneath the impact basin, assuming that the layer is mixed with the upper mantle in the process of shock wave propagation and subsequent mantle uplift.

4. Thermal Evolution Models

4.1. Impermeable Models

[28] We use impermeable models to investigate the effect of viscosity on the melt volume and the timing of volcanism. In the impermeable models, melting is allowed but melt migration is inhibited inside the partially molten regions. A temperature-dependent Newtonian viscosity is adopted,

$$\eta = \eta_o \exp(-C(T-T_o)) \quad (23)$$

where η and η_o are respectively the viscosity at a given point in the convecting region and the viscosity at zero

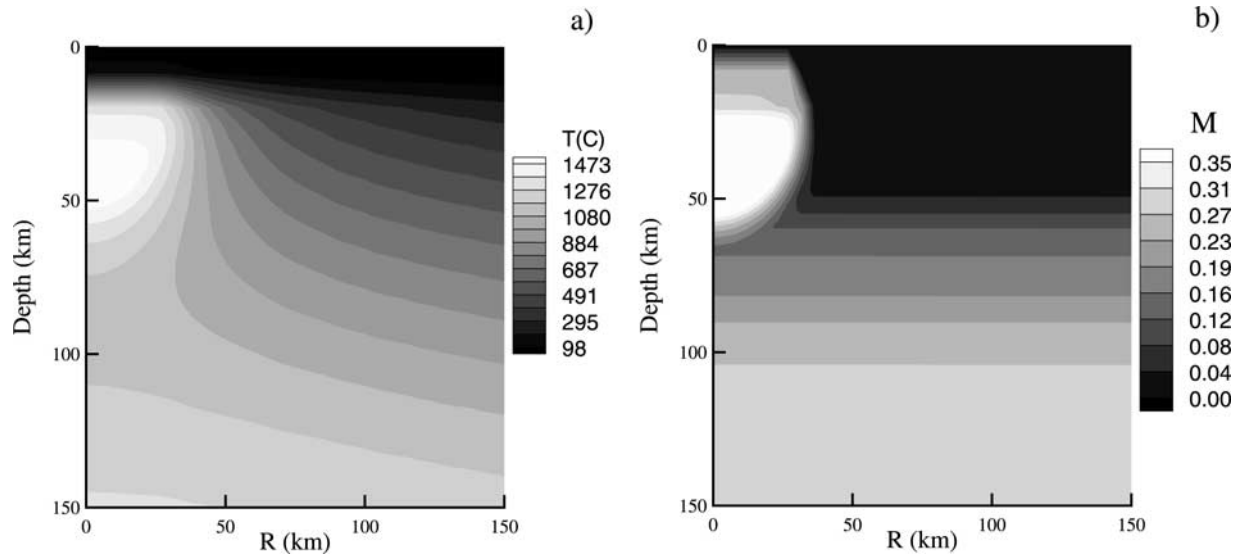


Figure 3. (a) Initial temperature and (b) melt depletion fields for an impermeable postimpact model with an impact basin of 600 km in diameter. Only the regions beneath and in the vicinity of the impact basin are shown.

temperature referred to as the referenced viscosity. $C = \ln(\Delta\eta)$, is a constant which depends on the assumed viscosity contrast, $\Delta\eta$, between the top and bottom of the calculation domain. To ensure that the crust does not participate in the mantle convection the viscosity of the crust is set to 10^{23} Pa s. A significant part of the viscosity variations occurs in the stagnant lid, and moderate viscosity variations occur within the convecting mantle where the adiabatic temperature changes only slightly. We note that the adiabatic temperature increases by only about 30 degrees from the surface to the center of the Moon. The viscosity varies by less than an order of magnitude across the convecting mantle in our successful models (Figure 2b). The impact-induced thermal perturbations further confine the region with high viscosity variations to shallower depths. Our viscosity model is similar to the one adopted by *Grasset and Parmentier* [1998] and *Reese et al.* [2004] for Martian mantle. *Reese et al.* [1999] showed that at large viscosity contrasts between the convecting mantle and the stagnant lid, the differences between Arrhenius [*Krato and Wu*, 1993] and exponential viscosity laws are less important for calculation of the interior temperature field. Also, *Grasset and Parmentier* [1998] showed that under stagnant lid convection regime with temperature-dependent viscosity and internal heating, similar to our lunar model, the mantle behaves as an isoviscous medium. In the above equation T and $T_0 (= 0^\circ\text{C})$ are normalized temperatures at a given point in the convecting region and at the surface, respectively. We ignore the pressure effects on viscosity because the pressure in the Moon is small and the pressure dependence of viscosity is probably negligible compared to its temperature dependence. Five different viscosity contrast models, models 1 to 5, are examined, where the ratio between the viscosity at the surface and at the bottom of the computation domain are 100, 500, 1000, 1500 and 2000, respectively. To name the models described in this paper consistently and easily, a model name consists of three parts; (1) the word “model” is preceded by a number specifying the viscosity

contrast used in the model, (i.e., model 1 to model 5 denote the viscosity contrasts of 100 to 2000 used in the models), (2) the letter I or P showing whether the model is impermeable or permeable and (3) the letter a, b, or c indicating the reference viscosity, 10^{23} , 10^{22} or 10^{24} Pa s used in the model. For example an impermeable model with viscosity contrast of 1000 and reference viscosity of 10^{23} Pa s is called model 3Ia.

[29] The laterally averaged temperature and melt depletion profiles immediately before the impact are determined through the thermal evolutions of the preimpact impermeable models, model 1Ia to model 5Ia. The temperature profiles of model 1Ia, model 3Ia, and model 5Ia are shown in Figure 2a. The solidus and liquidus of the mantle at 4.6 Gyr ago are also included in the figure. The temperature profiles of the other models are within the profiles shown in the figure. The solidus is used for the initial temperature of the models as mentioned before. Models 3Ia, 4Ia and 5Ia produce adiabatic mantle temperatures, whereas models 1Ia and 2Ia have temperature profiles far from adiabat. This is a direct result of a smaller Rayleigh number of the latter models that results in weaker circulations of the mantle and less cooling during the preimpact period of 600 My. Model 3Ia still has much higher temperature than the solidus within 100 to 400 km depths. The model is almost as hot as the mantle adiabat of 1350°C used by *Elkins-Tanton et al.* [2004], but colder than their higher adiabat of 1450°C . The authors argued that the adiabats are consistent with the experimentally determined multiple saturation points of mare basalt and picritic glasses. However, the experimental observations reveal the postimpact temperature of the source region which has already been heated by the impact (Figure 3), and not the preimpact upper mantle.

[30] The postimpact thermal evolution models are calculated starting at 4 Gyr ago and using the temperature distribution immediately after an impact. The initial melt depletion field of a postimpact model is the laterally averaged melt depletion field at the end of preimpact model

plus the impact-induced melt depletion and the melt depletion arising from the subsequent isostatic uplift of the mantle. Figure 3 shows the initial temperature and melt depletion fields of the postimpact model 3Ia which is impacted by an Imbrium-size projectile that created a basin of 600 km diameter. The impact heating increases the uppermost mantle temperature directly beneath the impact site by hundreds of degrees. The initial melt depletion field shows that the upper mantle is highly depleted because of the partial melting prior to the impact and further melting due to the impact heating and subsequent mantle uplift. This is the case for all models. We note that melting buffers temperature at a given point because of enthalpy of melting and, in the mean time, contributes significantly to the buoyancy of the partially molten zone.

[31] Figure 4a compares the postimpact cumulative melt volume produced by the five models. The models are calculated for an Imbrium-type impact basin. All five models have similar initial melt production (i.e., about $40,000 \text{ km}^3$) soon after the impact, due to impact-induced thermal perturbations, in situ depressurized melting, and subsequent mantle uplift, i.e., the combination of the second and third phases of melting mentioned above. As we will show later the volume of the initial melt is only about 2% of the cumulative melt volume produced by the successful model 3Ia. This is in agreement with observation [e.g., Boyce, 1976; Geiss *et al.*, 1977] but in contrast to the results of *Elkins-Tanton et al.* [2004], where about 98% of the cumulative melt is due to the in situ melting occurred almost immediately after the impact and the release of the melt existed prior to impact. The volume of the in situ melting in our models is smaller than that of models presented by *Elkins-Tanton et al.* [2004], because the upper mantle in our models is far more depleted during the preimpact thermal evolution and thus has high solidus temperature. Also, there is no pervasive melt in the upper mantle of our models prior to the impact. The major preimpact melting occurred very early in the history of the Moon and resulted in magma ocean and mantle differentiation. Because of the stratified nature of the depletion field in our models (Figure 3b), melt is produced in the upper mantle by pushing away the depleted upper mantle from beneath the impact basin and replacing it with less depleted mantle material from deeper interior by the whole mantle convection. This explains the observed delay of the major basaltic flows relative to the impact time. This fourth phase of melting starts at different times in the models. Models 1Ia and 2Ia produce the largest volume of melt because they have warmer mantle relative to models 3Ia, 4Ia and 5Ia (Figure 2a). The mantle convection in the preimpact history of model 1Ia and model 2Ia was not vigorous enough to cool the interior appreciably. The fourth phase of melting starts at about 3 Gyr ago (i.e., after 1 Gyr from the impact time) and continues afterward, too late and too long duration to explain the basaltic volcanism that actually peaked at about 3.6 Gyr ago and diminished by 3 Gyr ago [e.g., Head, 1976]. These two models are not viable. Model 4Ia produces very small volume of melt up to about 2.2 Gyr ago but a significant melt afterward, too late to explain the observation. The sudden strong increase of melt production at 1.8 Gyr ago is related to the vigorous global convection due to its low-viscosity mantle that results in global melting mainly far from the basin, i.e.,

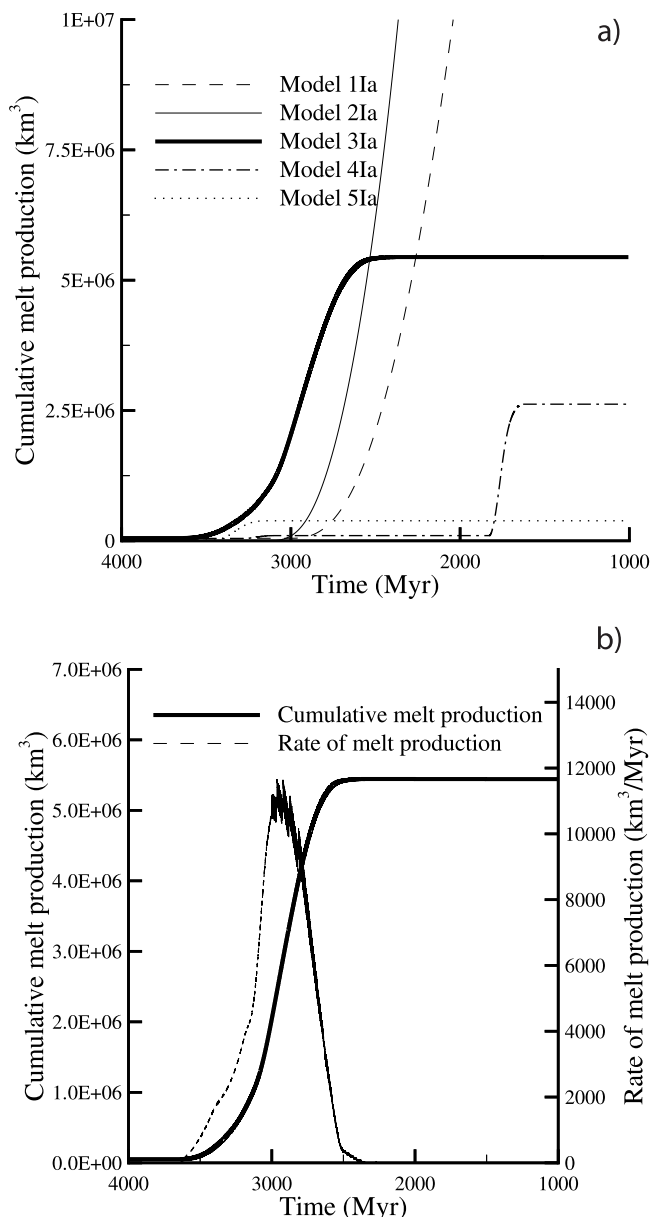


Figure 4. (a) Cumulative melt volume versus time for postimpact impermeable models 1Ia, 2Ia, 3Ia, 4Ia, and 5Ia. (b) Temporal variations of the cumulative melt volume and rate of melt production by the postimpact impermeable model 3Ia. Viscosity varies only with temperature. The impact basin diameter is 600 km. Horizontal axis is age in Myr. Read $1\text{E} + 07$ as 1×10^7 .

independent of impact. For model 5Ia, the peak melting happens at about 3.2 Gyr ago but the volume is not enough (about $384,000 \text{ km}^3$) to explain the observation. Model 3Ia seems to be reasonable as far as the melting time and amount of melt are concerned. Figure 4b shows the cumulative melt production and rate of melting in this model. The model starts producing a significant amount of melt at about 3.6 Gyr ago (Figures 4a and 4b), and its cumulative melt volume reaches a maximum value of $5 \times 10^6 \text{ km}^3$ at 2.8 Gyr ago. The average lava eruption rate at the surface of the Moon has been estimated to be $10^4 \text{ km}^3/\text{Myr}$ during

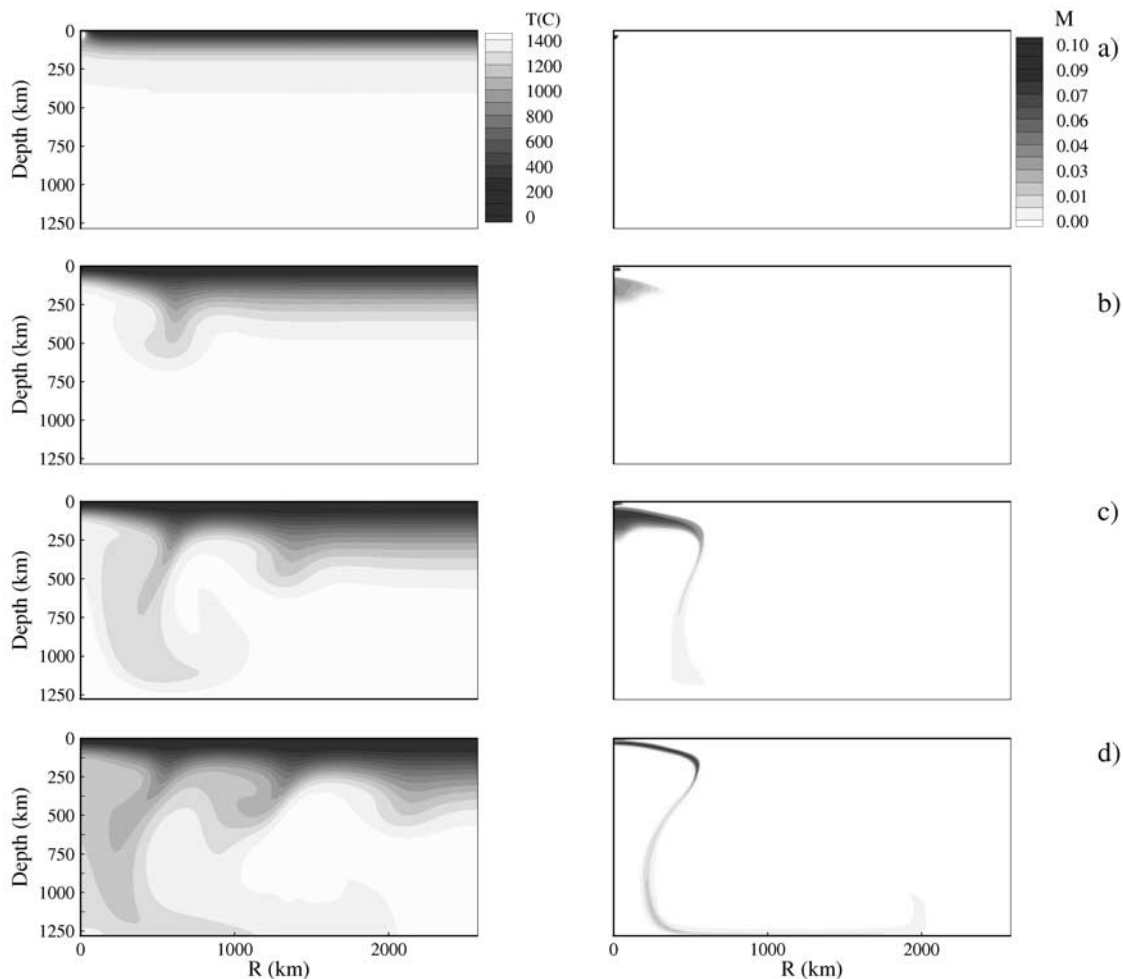


Figure 5. Four snapshots of temperature (left columns) and melt depletion (right columns) fields are shown for the impermeable model with viscosity contrast of 1000 (model 3Ia) and impact basin diameter of 600 km. From top to bottom the snapshots are for (a) 4000, (b) 3393, (c) 2785, and (d) 2177 Myr ago. Only the melt depletion field formed after the impact is shown in the right panels.

4.3–3.1 Gyr ago [e.g., *Spohn et al.*, 2001]. The melt production rate in the mantle is estimated to be 10^2 – 10^4 larger than the surface eruption [*Head and Wilson*, 1992] since most of the magma may not have erupted. Figure 4b shows that the melt production rate in the mantle for the impermeable model 3Ia is only slightly larger (about 1.2×10^4 km³/Myr) than the observed rate of lava eruption associated with the Imbrium impact. However, the peak melting occurs at about 3 Gyr ago, somewhat later than the observed volcanic peak [e.g., *Head*, 1976]. The results of the five models suggest that increasing viscosity contrast increases preimpact cooling and reduces the volume of melt produced in the postimpact period.

[32] The details of thermal state and melt production for model 3Ia are shown by several snapshots of temperature and melt depletion fields in Figure 5. Only melt depletion produced after impact is shown. The postimpact melt depletion field immediately after the impact (Figures 5a and 5d) shows that partial melting only occurs within very shallow depths where the impact-induced thermal perturbations are large. The melting shortly after the impact is due to

the combined effects of impact heating, depressurization caused by excavation, and mantle uplift. Figure 5b shows that a whole mantle convection beneath the impact basin has already started to create a sizable melt depletion zone and a ring of cold material at the edge of the basin at about 3.4 Gyr ago. The convection is further empowered (Figure 5c) by sinking of this cold ring, which in turn results in upwelling of warmer mantle, thus partial melting directly beneath the basin. With time, the sinking cold ring develops instabilities at large distances from the axis of the basin, but the viscosity structure of the model hampers vigorous convection and substantial melting off the impact basin (Figure 5d). The melt depletion fields at 3.4 Gyr (Figure 5b) and 2.8 Gyr ago (Figure 5c) show that the depth of partially molten zone increases with time, in general agreement with the geochemical observation [*Hiesinger et al.*, 1999], but not enough to explain the depth range of the source region of mare basalt [*Taylor*, 1982], especially if picritic glasses are originated in that region.

[33] The effects of the KREEP layer and the ejecta blanket on melt production are estimated by comparing

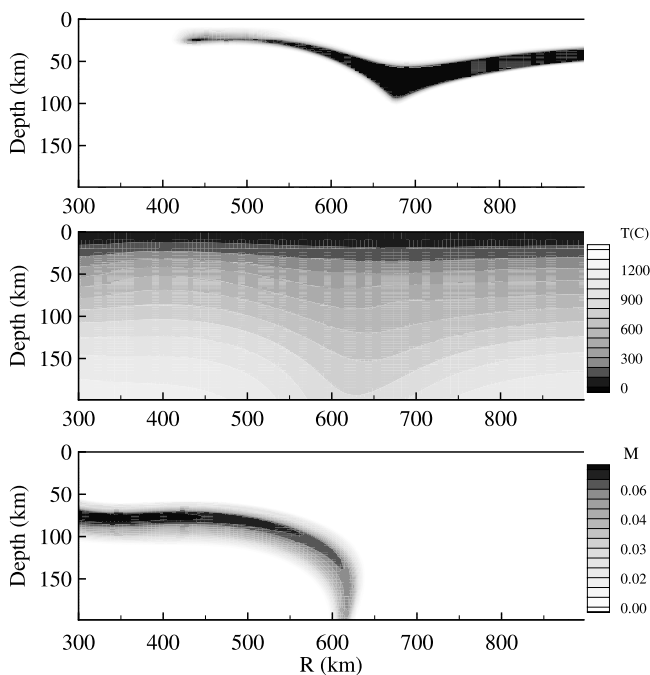


Figure 6. Snapshots of the tracer field representing the (top) KREEP layer, (middle) temperature, and (bottom) melt depletion fields beneath the ejecta blanket and surroundings at 2.2 Gyr ago. The snapshots are for model 3Ia with an impact basin diameter of 600 km.

the time evolution of the temperature and melt depletion fields of model 3Ia with the shape of its KREEP layer. In all of our models, the deformation of the KREEP layer is determined by tracking a tracer field representing the layer. The value of tracer field is one inside the KREEP layer and zero outside. The layer tracking is performed by solving the pure advection equation using MSOU method [Sweby, 1984]. A significant thickening of the KREEP layer occurs at a distance of 500 km from the basin axis and at about 2 Gyr ago (Figure 6), similar to that suggested by *Arkani-Hamed and Pentecost* [2001]. The temperature field shows no significant heating beneath the ejecta layer and melt depletion field is always negligible within and in the vicinity of the KREEP layer (Figure 6). This is also the case for other models with basin diameters of 300, 1200 and 2400 km and their corresponding permeable models. The KREEP layer does not contribute to melting, because the whole mantle convection does not allow accumulation of radiogenic thermal energy of the KREEP layer. We also examined an initial crustal thickness of 60 km and arrived at a similar conclusion. Our results do not agree with those of *Manga and Arkani-Hamed* [1991] and *Wieczorek and Phillips* [2000] models, which are based on pure heat conduction calculations. We conclude that in a convecting lunar mantle the KREEP layer and ejecta blanket have minor effects on melt production in the mantle.

4.2. Permeable Models

[34] *Ghods and Arkani-Hamed* [2002] showed that melt migration inside a partially molten part of a mantle plume can significantly increase the upwelling velocity of the

plume and its melt production. A second set of experiments is performed where we allow melt to migrate within the partially molten zone, and explore the effect of melt migration on the timing and amount of melt production. Figure 7a compares the cumulative melt production of model 3Ia and its permeable version, model 3Pa. The figure clearly shows that melt migration decreases the time between the start of the fourth phase of melting (i.e., at about 3.5 Gyr ago) and the maximum melt production (i.e., at about 3.2 Gyr ago), by about 400 Myr. This is because melt

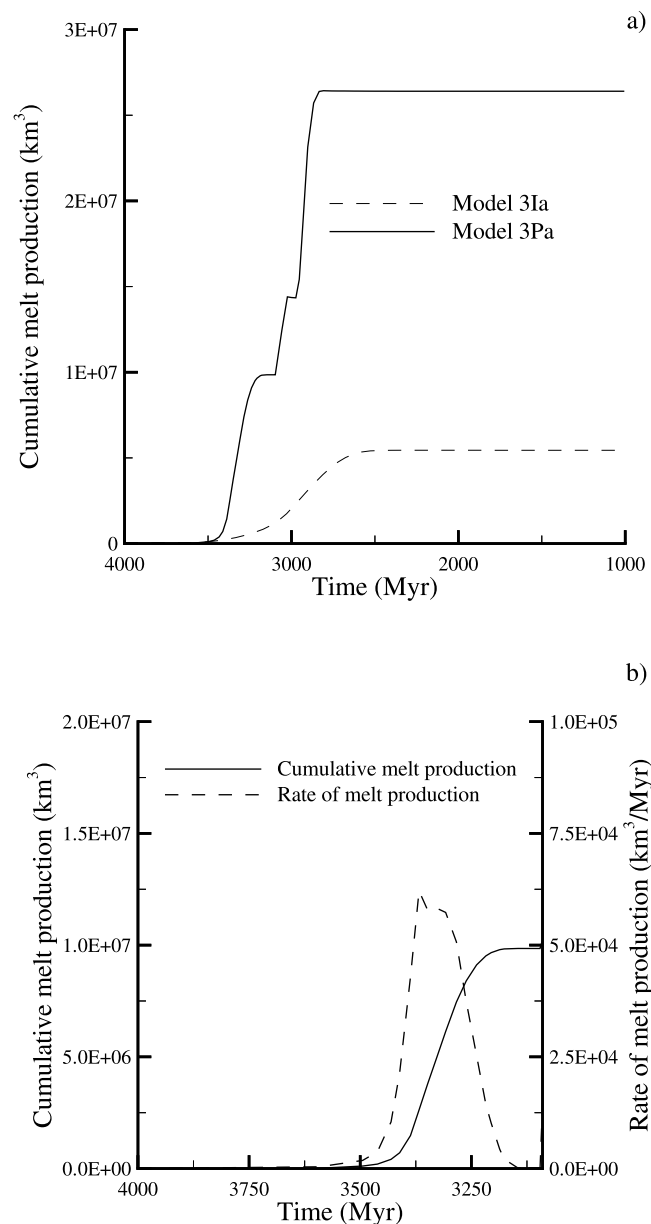


Figure 7. (a) Comparing time evolution of the cumulative melt production produced by permeable model 3Pa (solid line) and impermeable model 3Ia. (b) Temporal variations of cumulative melt volume and the rate of melt production by postimpact models 3Ia and 3Pa. Viscosity varies only with temperature, and impact basin diameter is 600 km. Horizontal axis is age in Myr.

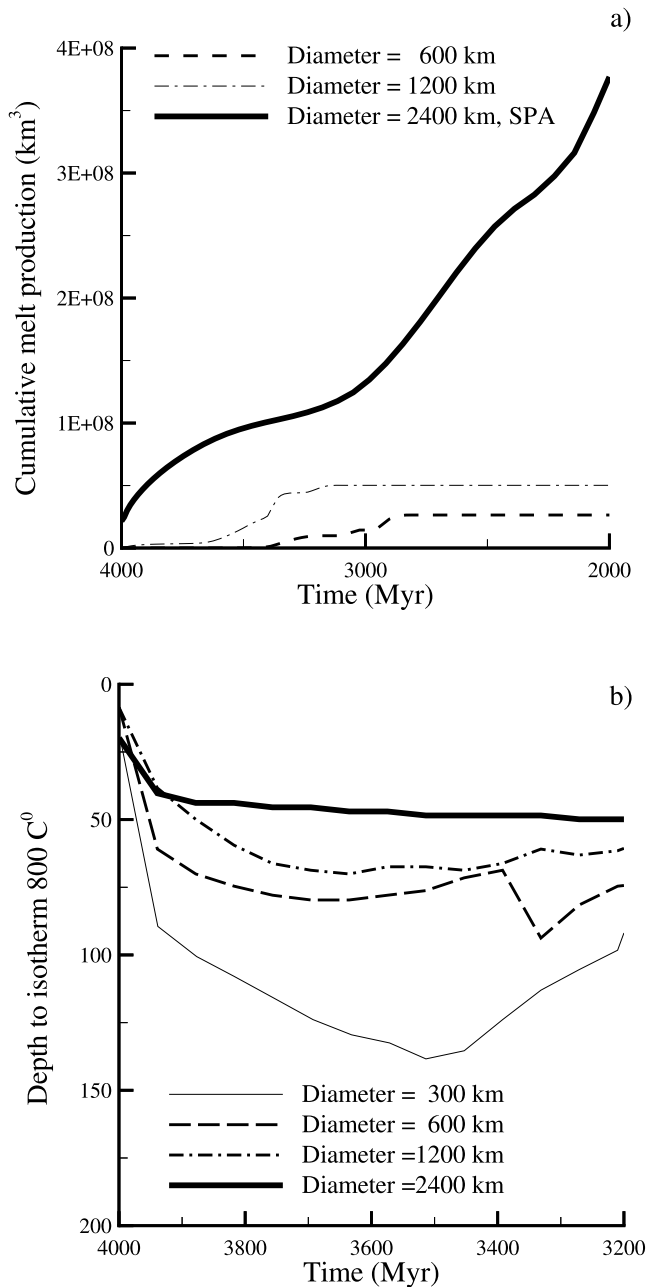


Figure 8. (a) Comparing the time evolution of the cumulative melt production of impact basins with diameters of 600, 1200, and 2400 km. Horizontal axis is age in Myr. (b) Time history of the depth to isotherm 800°C, representing the bottom of the elastic lithosphere for the impermeable models with impact basin diameters of 300, 600, 1200, and 2400 km. A maximum viscosity contrast of 1000 and reference viscosity of 10^{23} Pa s (model 3Pa) are used in the models. Horizontal axis is age in Myr. Except for the model with basin diameter of 2400 km, the rest are permeable models.

migration focuses melt retention buoyancy in the top portion of the upwelling mantle and increases the upwelling velocity. The increased velocity in turn reduces the time required for the materials from deep mantle to reach the upper mantle, thus hampering appreciable heat loss of the materials and enhancing the melt production. The maximum volume of melt in the fourth phase of melting of model 3Pa is about twice larger than that of model 3Ia. Unlike model 3Ia, model 3Pa develops a fifth phase of melting at about 3 Gyr ago in which low-percentage melting occurs far from the impact basin, over a rather large region. The melting is due to global convection caused by the descending plumes beneath the cold lithosphere. The two sudden jumps in the cumulative melt volume of model 3Pa (Figure 7) are related to off-basin melting caused by the global convection. Figure 7b shows the time history of the rate and cumulative volume of melt production for model 3Pa, which are comparable with the observed values of Imbrium basin. For clarity the time history is only shown up to the beginning of the fifth phase of melting. The maximum rate of melting of the permeable model 3Pa is about 6 times larger than that of the corresponding impermeable model 3Ia (Figure 4b).

4.3. Effects of Impact Size

[35] In the third set of models, we explore the effect of the impact size on the timing and melt production in the lunar mantle. The width of the continuous ejecta blanket is taken equal to the radius of the impact basin. Figure 8a compares the time history of cumulative melt volume produced by permeable models (model 3Pa) with impact basin diameters of 600 and 1200 km and a SPA-size impact basin of 2400 km diameter. Table 2 lists the delay time between impact time and start of volcanism, the total volume of melt at the end of the fourth phase of melting, and the volume of melt produced by the second and third phases of melting for models with basin diameters of 200, 300, 600, 1200 and 2400 km. The total volume of melt at the end of the fourth phase of melting corresponds to melting of the upwelling plume beneath the impact basin. The melt percentage of the fifth phase of melting is very low and far from the impact basin. Although there is no impact basin of 1200 km diameter on the Moon, we model it in order to illustrate more clearly the progression of the effect of impact size on the volume and duration of melt production. For the SPA-size model we only transfer 20% of the kinetic energy to thermal energy to account for the suggested oblique SPA impact [Schultz, 1997]. For models with 1200 and 2400 km diameters, the fourth phase of melting starts shortly after the third phase (Table 2). This is because the models with larger impact diameters have hotter and less viscous upper mantle beneath the impact basin and initiate the whole mantle convection sooner than other models. This set of models suggests that the larger the impact basin, the shorter is the delay between the impact and major volcanic flows. The melt volume produced in the first phase of melting for the SPA-size impact is the largest because the kinetic energy and the associated impact-induced thermal energy are the largest. Therefore the calculated volume of melt by our model suggests immediate and enormous flooding of the SPA basin. The large aspect ratio of 8 adopted for this model, the zero heat flux boundary condition imposed at the base of the

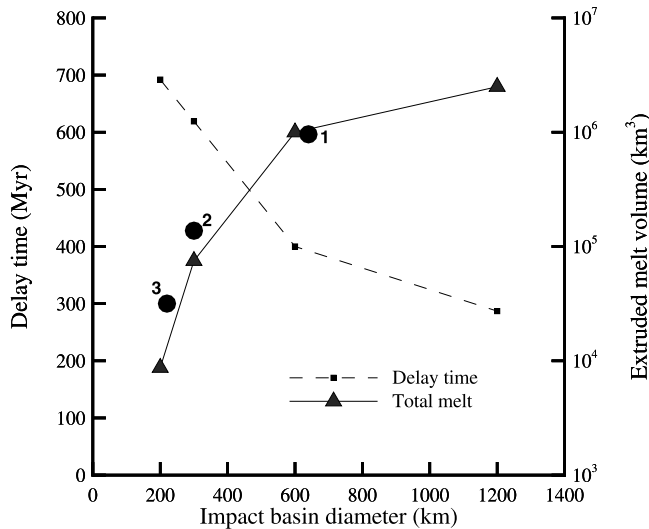


Figure 9. Total extrusive melt volume (solid line with triangular symbols) and the delay time for impact-induced volcanism (dashed line with square symbols) as calculated by our successful model 3Pa, versus the diameter of the impact basin. We assume that total extrusive melt volume is 10% of the total melt produced. The estimated basalt volumes [Solomon and Head, 1980] are shown as solid circles, where the number adjacent to each circle indicates the basin: 1, Imbrium; 2, Orientale; and 3, Grimaldi.

calculation domain and the depth of significant melting being limited to depths not greater than 300 km suppress the differences between the cylindrical coordinate results and those that would be obtained using spherical shell model. The total melt volume calculated by our axisymmetric cylindrical coordinate system model is likely a reasonable estimate for that of a spherical coordinate model. We also investigated permeable models with impact basin diameters of 100 km, 200 km and 300 km, representing the Copernicus-type crater, Girmaldi- and Orientale-type basins, respectively. They are not shown in Figure 8a. The former does not produce any melt and the Girmaldi- and Orientale-type models produce a cumulative total melt volume of about 0.87×10^5 and 0.75×10^6 km³ (Table 2). Figure 9 shows the calculated delay time and total extrusive melt volume versus impact diameter. The total extrusive melt volume is assumed to be 10% of the total volume of melt produced by a given

model. Similar ratio was also adopted by *Elkins-Tanton et al.* [2004]. Figure 9 also shows the estimated observed volume of mare basalts [Solomon and Head, 1980]. In our models the diameters of the inner rings of the basins, approximated by 200 km, 300 km and 600 km for Grimaldi, Orientale and Imbrium basins, represent the basin size. The calculated total extrusive volumes of melt are in good agreement with the observed volumes. The volume of the first phase of melting for smaller impact basins is negligible (Table 2).

4.4. Supporting Mascons

[36] A model is viable if in addition to the production of a reasonable volume of melt and satisfying the starting time and duration of melting, it also produces a strong lithosphere capable of supporting the extra masses associated with the near side basins, the mascons, for the last 3 Gyr. Figure 8b shows the depth to 800°C isotherm, assumed to represent the elastic-ductile transition temperature of the lithosphere, at the center of basin for the four models with basin diameters of 300, 600, 1200 and 2400 km. The first three of the models are permeable. However, because of computational difficulty in handling large percentage of melt production in the last model, we could only calculate the time history of the depth to elastic-ductile transition for the impermeable version of the SPA-size model. Given the fact that the delay between impact and the fourth phase of melting for this model is very small, and also the volume of melt produced by this model is already very huge, we suspect that permeable and impermeable SPA models have comparable time history of the depth to elastic-ductile transition. The figure shows that the thickness of the elastic lithosphere beneath the basins decreases with the increase of the basin size. The lithosphere beneath the SPA basin is thinner than that beneath 1200 km impact basin despite the assumption of an oblique impact for SPA where only 20% of the kinetic energy of the impactor is converted to heat. The figure demonstrates that the elastic lithosphere beneath Imbrium-type basins, such as Imbrium, Serenitatis, Crisium, Humorum, Nectaris and Homboltianum, is comparable to the elastic lithosphere thickness required to support the extra masses associated with these basins (see *Arkani-Hamed* [1998] and many references there). On the other hand, the elastic lithosphere beneath SPA basin remains thin, unable to support extra mass possibly produced after the impact. The fundamental wavelength of the possible surface load is about 2 orders of magnitude longer than the thickness of the elastic lithosphere. The asymmetric

Table 2. Delay Time Between Impact Time and Volcanism, Total Volume of Melt Production at the End of Fourth Phase of Melting, and Melt Volume Produced by Second and Third Phases of Melting for Models With Different Impact Basin Diameters^a

Diameter, km	Delay Time, Myr	Total Melt Volume, km ³	Second and Third Phases of Melting, km ³
200	692	0.87×10^5	0
300	619	0.75×10^6	0
600	400	1.0×10^7	8.0×10^3
1200	287	5.0×10^7	3.7×10^6
2400	0	40.0×10^7	2.1×10^7

^aAll models are permeable except for SPA-size impact basin, and all use a temperature-dependent viscosity with a viscosity contrast of 1000 and reference viscosity of 10^{23} Pa s, corresponding to model 3Pa.

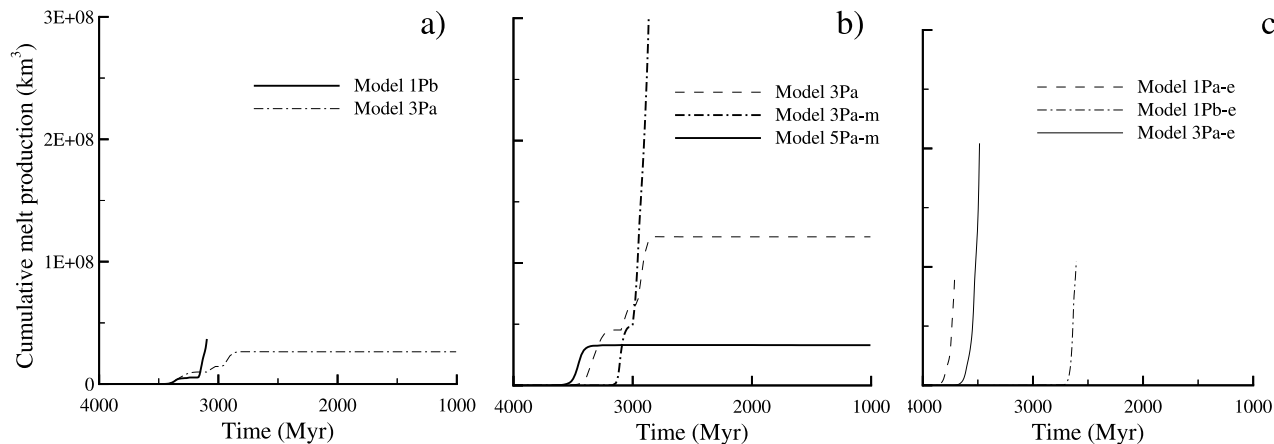


Figure 10. (a) Cumulative melt volume versus time for postimpact models 1Pb and 3Pa. Viscosity varies only with temperature. (b) Cumulative melt volume versus time for postimpact models 3Pa-m and 5Pa-m with a temperature- and melt-dependent viscosity. The cumulative melt volume versus time for model 3Pa with temperature-dependent viscosity is shown (dashed curve) for comparison. (c) Cumulative melt volume versus time for postimpact models 1Pa-e, 1Pb-e, and 3Pa-e with temperature-dependent viscosity, assuming 35% of the total radioactive elements is in the mantle. In all of the models, the impact basin diameter is 600 km, and the horizontal axis is age in Myr.

geometry of the surrounding highlands of SPA impact basin led *Schultz* [1997] to suggest that SPA impact was oblique ($< 30^\circ$), and could not penetrate into the mantle. Nonetheless, the huge impact heating is expected to initiate a vigorous whole mantle convection [see also *Arkani-Hamed and Pentecost*, 2001] and produce a huge amount of melt on the basis of our results. Similar results are also expected from other models [e.g., *Manga and Arkani-Hamed*, 1991; *Elkins-Tanton et al.*, 2004]. One plausible scenario is that the interior of the Moon was heterogeneous even after differentiation that resulted in a thicker crust in the far side compare to that in the near side. However, the impact is so enormous that even an oblique impact of SPA size would be capable of thinning the crust directly beneath the impact site and producing significant partial melting in the deeper parts of the upper mantle. The head pressure of the deep seated melt would be sufficient to initiate pervasive volcanism over the thinned crust. It seems possible that the basaltic flows that filled the basin in the early stages were rapidly isostatically compensated and the basin floor has been largely covered by the ejecta of the later impacts. Although our model cannot explain the apparent absence of substantial basaltic flow in SPA basin, it can explain the lack of mascon associated with the basin.

5. Effects of Physical Parameters

[37] To evaluate the sensitivity of our models to the reference viscosity (η_o), we have calculated the time history of the cumulative melt production for permeable models 1, 3, and 5 using two extra values of η_o , 10^{22} and 10^{24} Pa s. The reference viscosity, η_o , in all of our previous models was 10^{23} Pa s. Again an impact basin diameter of 600 km is considered. The new sets of models are combinations of the

preimpact and postimpact models where only the postimpact parts of them are considered to be permeable. The impact-induced upwelling plume for permeable models with reference viscosity of 10^{24} Pa s (i.e., models 1Pc, 3Pc and 5Pc) does not produce a fourth phase melting, implying that the models are not viable. Among the models with reference viscosity of 10^{22} Pa s (i.e., models 1Pb, 3Pb, and 5Pb), only model 1Pb produces significant melt with appropriate timing (Figure 10a), similar to the permeable model 3Pa (Figures 10a and 7a). The melting far from the basin, the off basin melting, occurs in both models around 3.2 Gyr ago. However, because of its large Ra number model 1Pb develops strong global circulations with many ascending and descending plumes, and a larger amount of off basin melting than model 3Pa. We conclude that permeable model 3Pa with reference viscosity of 10^{23} is more preferable.

[38] The melt retained within the solid matrix reduces the viscosity of the matrix by 1–2 orders of magnitude depending on the percentage of the retained melt [*Hirth and Kohlstedt*, 1995]. However, because of melt migration in the permeable models, only a minor amount of melt remains in the melt depleted regions, the major part of the melt pounds at the top of the ascending plume and the softening effect of the melt is mainly limited to a very small region on the top of the plume. The minor softening of the depleted region has limited effects on the dynamics of the upwelling plume, whereas the large buoyancy of the melt pounded at the top causes the plume to rise quickly.

[39] Experimental results [*Hirth and Kohlstedt*, 1996] suggest that extraction of water from mantle due to partial melting may increase the viscosity of the solid residue matrix by 2–3 orders of magnitude. To investigate the effect of such a viscosity increase, we calculate the melt production for permeable models 1Pa, 3Pa, and 5Pa while

incorporating the viscosity increase of the solid residue matrix due to partial melting. An impact basin diameter of 600 km is used in the models. The viscosity of the models is increased linearly with the increase of melt depletion. The solid residue matrix viscosity increases by an order of magnitude for a maximum melting of 25%. Figure 10b compares the postimpact cumulative melt production of the permeable models model 3Pa-m and model 5Pa-m, corresponding to model 3Pa and model 5Pa, which take in to account the effect of melting on the viscosity of the residue solid matrix. For easy comparison, the figure also includes the postimpact cumulative melt production for the original permeable model 3Pa. The viscosity increase of the residue solid matrix delays the formation of the upwelling plume and its partial melting by about 250 Myr, and increases the volume of melt produced in the off basin melting. The effective smaller Ra number of the model allows for less cooling during the preimpact time and thus a hotter mantle at the impact time, which in turn causes a large volume of melt. Unlike model 3Pa and model 3Pa-m (Figure 10b), model 5Pa-m produces no off basin melting, it is regarded as an acceptable model.

[40] In all of the previous models we assumed a very high percentage of radioactive heat generating elements (90%) in the crust and the KREEP layer, in close agreement with *Binder and Lange's* [1980] model. The assumption implies an initial whole mantle magma ocean where radioactive elements effectively partitioned to the shallow depths. To test the sensitivity of our results to the initial distribution of radioactive elements, we calculate a set of preimpact and postimpact models where the concentration of radioactive elements of KREEP layer is reduced from 60% to 35%, and the mantle is assigned to have 35% of the total radioactive elements, similar to that of *Schubert et al.'s* [1980] model. For the ease of naming of the new models, we add "e" to the end of a given model name. The new permeable models 1, 3 and 5 are calculated for reference viscosities of 10^{22} , 10^{23} and 10^{24} while using an impact basin diameter of 600 km. Models 1Pc-e, 2Pc-e and 3Pc-e do not result in the fourth phase of melting. Figure 10c shows the time history of cumulative melt production for model 1Pb-e, model 1Pa-e, and model 3Pa-e. Model 1Pc-e and model 3Pa-e result in acceptable timing for the start of melt production (about 150 and 300 Myr after the impact, respectively) but the volume of melt increases asymptotically within the period we run the models and becomes as large as $2 \times 10^8 \text{ km}^3$. The evolutions of the melt depletion and temperature fields for the models show that the melt produced by the models is mostly related to the fourth phase of melting. The excessively large volume of melt production is due to the hotter (i.e., by about 50 K) initial postimpact temperature of the models. The hotter mantle of the models increases the depth of melting, by about 100 km, and considerably enlarges the size of the impact-induced upwelling plume.

6. Conclusions

[41] In this paper we evaluate the contribution of impact-induced whole mantle convection to the volcanism on the Moon using a 2-D axisymmetric cylindrical coordinate system and two-phase flow calculations. Our thermal evolution models span from preimpact to postimpact times, and

include impermeable and permeable mantle. The mantle has temperature- and composition-dependent viscosity and temperature-dependent thermal conductivity. We show that a delayed phase of mare basalt volcanism is a direct consequence of the delayed initiation of the whole mantle convection. Melt migration inside partially molten zone in the mantle reduces the time between the initiation of volcanism and its peak flow period. Similar results are obtained because of increase of impact size. We investigated sensitivity of our results to different viscosity values. The models where the mantle viscosity was reduced by a factor of 1000 relative to the viscosity at the surface were found viable. A permeable model with such a viscosity variations not only can explain the amount of observed basaltic flows in the Imbrium-size basins, but can also explain the observed delayed starting time and the duration of the major flooding of the basins. Such models also allow a thick rigid lithosphere to develop directly beneath the basin and support the mascon subsequently formed in the basin. Our models can also explain the minor flooding of Orientale-type basins and the lack of flooding of Copernicus-type craters. However, our model for SPA impact basin produces a huge amount of melt in the mantle, and thus major flooding expected, which does not agree with the observed minor basaltic flows inside the basin. The SPA basin remains unexplained by our model as well as by models presented by other investigations. However, on the basis of our model the huge flooding of this basin does not produce mascon because of the thin and hot lithosphere beneath the basin that is incapable of supporting surface/crustal loads. This aspect of our model is in good agreement with the lack of mascon associated with this basin.

[42] **Acknowledgments.** A.G. thanks Ministry of Science, Research and Technology of Iran for supporting the parallel computing facilities at IASBS under grant 1026B (503495). The research was partly supported by the Natural Sciences and Engineering Research Council (NSERC) of Canada grant to J.A.H. We would like to thank the Associate Editor for useful suggestions and the two reviewers, L. T. Elkins-Tanton and V. S. Solomatov, for their constructive comments.

References

- Arkani-Hamed, J. (1973), On the formation of the lunar mascons, *Proc. Lunar Sci. Conf. 4th*, 2673–2684.
- Arkani-Hamed, J. (1974), Effect of a giant impact on the thermal evolution of the Moon, *Moon*, 9, 183–209.
- Arkani-Hamed, J. (1998), The lunar mascons revisited, *J. Geophys. Res.*, 103, 3709–3739.
- Arkani-Hamed, J., and A. Pentecost (2001), On the source region of the lunar mare basalt, *J. Geophys. Res.*, 106, 14,691–14,700.
- Arkani-Hamed, J., W. L. Sjogren, and A. S. Konopliv (1999), On the equipotential surface hypothesis of lunar maria floors, *J. Geophys. Res.*, 104, 5921–5931.
- Bercovici, D., Y. Ricard, and G. Schubert (2001), A two phase model of compaction and damage: 1. General theory, *J. Geophys. Res.*, 106, 8887–8906.
- Binder, A. B., and M. Lange (1980), On the thermal history, thermal state, and released tectonism of a Moon of fission origin, *J. Geophys. Res.*, 85, 3194–3208.
- Bjorkman, M. D., and K. A. Holsapple (1987), Velocity scaling impact melt volume, *Int. J. Eng.*, 5, 155–163.
- Boyce, J. M. (1976), Ages of flow units in the lunar near side maria based on Lunar Orbiter IV photographs, *Proc. Lunar Sci. Conf. 7th*, 2717–2728.
- Cattermole, P. (1996), *Planetary Volcanism*, 2nd ed., John Wiley, Hoboken, N. J.
- Ceuleneer, G., and M. Rabinowicz (1992), Mantle flow and melt migration beneath oceanic ridges: Models derived from observations in ophiolites, *Geophys. Monogr. Ser.*, vol. 71, pp. 123–154, AGU, Washington, D. C.

- Cheadle, M. J. (1993), The physical properties of texturally equilibrated partially molten rocks, *Eos Trans. AGU*, 74, 283.
- Delano, J. W., and K. Livì (1981), Lunar volcanic glasses and their constraints on mare petrogenesis, *Geochim. Cosmochim. Acta*, 45, 2137–2149.
- Elkins-Tanton, L. T., B. H. Hager, and T. L. Grove (2004), Magmatic effects of the lunar late heavy bombardment, *Earth Planet. Sci. Lett.*, 222, 17–27.
- Geiss, J., P. Eberhardt, N. Groegler, S. Guggisberg, P. Maurer, and A. Stettler (1977), Absolute time scale of lunar mare formation and filling, *Philos. Trans. R. Soc. London, Ser. A*, 285, 151–158.
- Ghods, A., and J. Arkani-Hamed (2000), Melt migration beneath mid-ocean ridges, *Geophys. J. Int.*, 140, 687–697.
- Ghods, A., and J. Arkani-Hamed (2002), Effect of melt migration on the dynamics and melt generation of diapirs ascending through asthenosphere, *J. Geophys. Res.*, 107(B1), 2026, doi:10.1029/2000JB000070.
- Ghods, A., and J. Arkani-Hamed (2004), The formation of the lunar and Martian mascons, *Eos Trans. AGU*, 85(47), Fall Meet. Suppl., Abstract P23A-0230.
- Grasset, O., and E. M. Parmentier (1998), Thermal convection in a volumetrically heated, infinite Prandtl number fluid with strongly temperature-dependent viscosity: Implication for planetary thermal evolution, *J. Geophys. Res.*, 103, 18,171–18,181.
- Head, J. W. (1976), Lunar volcanism in space and time, *Rev. Geophys.*, 14, 265–300.
- Head, J., and L. Wilson (1992), Lunar mare volcanism: Stratigraphy, eruption conditions, and the evolution of the secondary crusts, *Geochim. Cosmochim. Acta*, 56, 2155–2175.
- Heiken, G., D. Vaniman, and B. M. French (1991), *Lunar Sourcebook: A User's Guide to the Moon*, Cambridge Univ. Press, New York.
- Hiesinger, H. R. Jaumann, G. Neukum, and J. Head (1999), Lunar mare volcanism: Age, composition, and flux, *Geophys. Res. Abstr.*, 1, 735.
- Hirth, G., and D. L. Kohlstedt (1995), Experimental constraints on the dynamics of the partially molten upper mantle: 2. Deformation in the dislocation creep regime, *J. Geophys. Res.*, 100, 1981–2002.
- Hirth, G., and D. Kohlstedt (1996), Water in the oceanic upper mantle: Implications for rheology, melt extraction and the evolution of the lithosphere, *Earth Planet. Sci. Lett.*, 144, 93–108.
- Holsapple, K. A. (1993), The scaling of impact processes in planetary sciences, *Annu. Rev. Earth Planet. Sci.*, 21, 333–373.
- Ivanov, B. A. (2001), Mars/Moon cratering rate ratio estimates, *Lunar Planet. Sci. [CD-ROM]*, XXXII, abstract 1249.
- Kohlstedt, D. L. (1992), Structure, rheology and permeability of partially molten rocks at low melt fractions, in *Mantle Flow and Melt Generation*, *Geophys. Monogr. Ser.*, vol. 71, edited by J. Phipps Morgan, D. K. Blackman, and J. M. Sinton, pp. 103–121, AGU, Washington, D. C.
- Konopliv, A. S., A. B. Binder, L. L. Hood, A. B. Kucinkas, W. L. Sjorgen, and J. G. Williams (1998), Improved gravity field of the Moon from Lunar Prospector, *Science*, 281, 1476–1480.
- Krato, S.-I., and P. Wu (1993), Rheology of the upper mantle: A synthesis, *Science*, 260, 771–778.
- Longi, J. (1992), Experimental petrology and petrogenesis of mare volcanism, *Geochim. Cosmochim. Acta*, 56, 2235–2251.
- Manga, M., and J. Arkani-Hamed (1991), Remelting mechanisms for shallow source regions of mare basalts, *Phys. Earth Planet. Inter.*, 68, 9–31.
- McKenzie, D. P. (1984), The generation and compaction of partially molten rock, *J. Petrol.*, 25, 713–765.
- McKenzie, D., and M. J. Bickle (1988), The volume and composition of melt generated by extension of lithosphere, *Petrol. J.*, 29, 625–679.
- Melosh, H. J. (1989), *Impact Cratering: A Geologic Process*, Oxford Univ. Press, New York.
- Melosh, H. J., and B. A. Ivanov (1999), Impact crater collapse, *Annu. Rev. Earth Planet. Sci.*, 27, 385–415.
- Mohit, P. S., and J. Arkani-Hamed (2004), Impact demagnetization of the Martian crust, *Icarus*, 168, 305–317.
- Nicolas, A. (1990), Melt extraction from mantle peridotites: Hydrofracturing or porous flow consequences on oceanic ridge activity, in *Magma Transport and Storage*, edited by M. P. Ryan, pp. 160–174, John Wiley, Hoboken, N. J.
- Nyquist, L. E., and C.-Y. Shih (1992), The isotopic record of lunar volcanism, *Geochim. Cosmochim. Acta*, 56, 2213–2234.
- O'Keefe, J. D., and T. J. Ahrens (1977), Impact-induced energy partitioning, melting, and vaporization on the terrestrial planets, *Proc. Lunar Sci. Conf. 8th*, 3357–3374.
- Patankar, S. V. (1980), *Numerical Heat Transfer and Fluid Flow*, 329 pp., Taylor and Francis, Philadelphia, Pa.
- Pierazzo, E., A. M. Vickery, and H. J. Melosh (1997), A reevaluation of impact melt production, *Icarus*, 127, 408–423.
- Presnall, D. C., and M. J. Walter (1993), Melting of forsterite, Mg₂SiO₄, from 9.7 to 16.5 GPa, *J. Geophys. Res.*, 98, 19,777–19,783.
- Reese, C. C., V. S. Solomatov, and L.-N. Moresi (1999), Non-Newtonian stagnant lid convection and magmatic resurfacing on Venus, *Icarus*, 139, 67–80.
- Reese, C. C., V. S. Solomatov, and J. R. Baumgardner (2002), Survival of impact-induced thermal anomalies in the Martian mantle, *J. Geophys. Res.*, 107(E10), 5082, doi:10.1029/2000JE001474.
- Reese, C. C., V. S. Solomatov, J. R. Baumgardner, and D. R. Stegman (2004), Magmatic evolution of impact-induced Martian mantle plumes and the origin of Tharsis, *J. Geophys. Res.*, 109, E08009, doi:10.1029/2003JE002222.
- Runcom, S. K. (1974), On the origin of mascons and moonquakes, *Proc. Lunar Sci. Conf. 5th*, 3115–3126.
- Schatz, J. F., and G. Simmons (1972), Thermal conductivity of Earth material at high temperatures, *J. Geophys. Res.*, 77, 6966–6983.
- Schmidt, R. M., and K. R. Housen (1987), Some recent advances in the scaling of impact explosion cratering, *Int. J. Impact Eng.*, 5, 543–560.
- Schubert, G., D. Stevenson, and P. Cassen (1980), Whole planet cooling and the radiogenic heat source contents of the Earth and Moon, *J. Geophys. Res.*, 85, 2531–2538.
- Schultz, P. H. (1997), Forming the South-Pole Aitken basin: The extreme games, *Proc. Lunar Planet. Sci. Conf. 28th*, 259.
- Smith, D. E., M. T. Zuber, G. A. Neumann, and F. G. Lemoine (1997), Topography of the Moon from the Clementine lidar, *J. Geophys. Res.*, 102, 1591–1611.
- Solomon, S. C. (1975), Mare volcanism and lunar crustal structure, *Proc. Lunar Sci. Conf. 6th*, 1021–1042.
- Solomon, S. C., and J. W. Head (1980), Lunar mascon basins: Lava filling, tectonics, and evolution of the lithosphere, *Rev. Geophys.*, 18, 107–141.
- Sparks, D. W., and E. M. Parmentier (1994), The generation and migration of partial melt beneath oceanic spreading centers, in *Magmatic System*, edited by M. P. Ryan, pp. 55–76, Elsevier, New York.
- Spohn, T., W. Konrad, D. Breuer, and R. Ziethe (2001), The longevity of lunar volcanism, Implications of thermal evolution calculations with 2D and 3D mantle convection models, *Icarus*, 149, 54–65.
- Sweby, P. K. (1984), High resolution schemes using flux limiters for hyperbolic conservation laws, *SIAM J. Numer. Anal.*, 21, 995–1001.
- Taylor, S. R. (1982), *Planetary Science: A Lunar Perspective*, Lunar and Planet. Inst., Houston, Tex.
- Von Bagen, N., and H. S. Waff (1986), Permeabilities, interfacial areas and curvatures of partially molten systems: Results of numerical computations of equilibrium microstructures, *J. Geophys. Res.*, 91, 9261–9276.
- Warren, P. H., and K. L. Rasmussen (1987), Megaregolith insulation, internal temperatures, and bulk Uranium content of the Moon, *J. Geophys. Res.*, 92, 3453–3465.
- Warren, P. H., and J. T. Wasson (1979), The origin of KREEP, *Rev. Geophys.*, 17, 73–88.
- Wieczorek, M. A., and R. J. Phillips (2000), The Precellarum KREEP Terrane: Implications for mare volcanism and lunar evolution, *J. Geophys. Res.*, 105, 20,417–20,430.

J. Arkani-Hamed, Department of Earth and Planetary Sciences, McGill University, 3450 University Street, Montreal, QC, Canada H3A 2A7.

A. Ghods, Institute for Advanced Studies in Basic Sciences, P. O. Box 45195-1159, Zanjan 45195, Iran. (aghods@iasbs.ac.ir)